# Cross section for Rydberg antihydrogen production via charge exchange between Rydberg positroniums and antiprotons in a magnetic field

D. Krasnický,[1] R. Caravita,[1] C. Canali,[2] and G. Testera[3,*]

[1]*Istituto Nazionale di Fisica Nucleare (INFN) Genoa and Department of Physics, University of Genoa via Dodecaneso 33, 16146 Genoa, Italy*

[2]*Istituto Italiano di Tecnologia Via Morego 30, 16163 Genoa, Italy*

[3]*Istituto Nazionale di Fisica Nucleare (INFN) Genoa, via Dodecaneso 33, 16146 Genoa, Italy*

(Received 10 April 2016; published 30 August 2016)

The antihydrogen formation by charge exchange between cold antiprotons and Rydberg positronium $P_s^*$ is studied by using the classical trajectory Monte Carlo method. In the absence of external magnetic field the cross section scaled by the fourth power of the $P_s^*$ principal quantum number $n_{P_s}$ shows a universal behavior as a function of the ratio $k_v$ between the velocity of the $P_s$ center of mass and that of the positron in the classical circular orbit. At low velocity, below about $k_v \simeq 0.2$–$0.3$, we show for Rydberg positronium that the cross section increases as $1/k_v^2$ or, in an equivalent way, as $1/E_{P_s}^{cm}$ with $E_{P_s}^{cm}$ being the $P_s^*$ center-of-mass energy. In this regime the distribution of the principal quantum number of the antihydrogen state is narrow and it shows a peak at about $\sqrt{2}n_{P_s}$ while at higher $k_v$ values a broad distribution of antihydrogen states is produced. The study of the collision process in the presence of moderate magnetic field (0.5–2 T) shows that there is an experimentally interesting region of $k_v$ with the cross section slightly higher than that in the absence of field. However the presence of a magnetic field changes significantly the cross section behavior as a function of $k_v$, especially at low velocities, where reductions of the cross sections and deviations from the $1/k_v^2$ ($1/E_{P_s}^{cm}$) are observed. Our calculations show a dependance of the cross section upon the angle between the magnetic field and the flight direction of the incoming $P_s^*$.

DOI: 10.1103/PhysRevA.94.022714

## I. INTRODUCTION

Antihydrogen atoms are a powerful physical system for accurate tests of some of the fundamental principles of physics. The precision measurement of the transition energies of the antihydrogen levels (especially the 1S-2S line or the hyperfine splitting of the fundamental state) and the comparison with the corresponding ones of hydrogen could result in the most precise test of the *CPT* symmetry for baryons ever performed [1]. In addition the direct measurement of the Earth's gravitational acceleration $g$ on antihydrogen would allow us to probe the validity of the weak equivalence principle (WEP) for a system made only by antimatter [2]. These two principles are related to the foundations of quantum field theory (*CPT*) and of general relativity (WEP) and presently no one has ever observed a *CPT* violation, nor a process in which WEP is not satisfied [3]. However, the search for any possible tiny violation is of interest as its discovery would be a signal of new physics [4].

The formidable accuracies reached in the field of hydrogen spectroscopy [5] and gravitational measurements with cold atoms [6] represent the long term goal of the antihydrogen experiments. Presently there is still an experimental gap to be bridged between the cold atom and cold antiatom physics which is dominated primary by the different values of the temperature of the available samples but also by the difference in the number of available particles. While ordinary atoms are at one's disposal in large quantities and can be cooled to $\mu$K or nK temperature, only small numbers of antihydrogen atoms are presently produced with temperature in the range of K [7]. High sensitivity spectroscopy and precision gravitational measurements on antihydrogen both demand us to prepare antiatoms with sub-K temperature, possibly in the range of mK or below.

After the production of antihydrogen with a temperature of about some tens of Kelvin by the ATHENA [8] and ATRAP [9] experiments in 2002, the present challenge of the ongoing experimental activity is towards the production of antiatoms as cold as possible and in large quantities. The efforts are focused on trapping antihydrogen in a magnetic trap as in the ALPHA [10] or ATRAP [11] experiments or producing a cold beam as in the AEgIS [2] or ASACUSA [12] ones or, finally, on getting cold antihydrogen through the intermediate formation of charged antimatter ions as in the GBAR project [13].

Antihydrogen atoms are produced by three-body recombination of antiprotons and positrons trapped and cooled in electromagnetic traps [14] or by charge exchange between Rydberg positronium ($P_s^*$) and antiprotons. The last reaction

$$P_s^* + \bar{p} \rightarrow \bar{H}^* + e^-, \tag{1}$$

pioneered by the ATRAP collaboration [15], is the main antihydrogen formation mechanism in the AEgIS experiment.

In this paper we present detailed results about the calculation of the charge-exchange cross section obtained with a classical trajectory Monte Carlo method (CTMC). We assumed that antiprotons are at rest and we studied the collision process as a function of the positronium center-of-mass velocity for various principal quantum numbers of the positronium $n_{P_s}$. We first performed the calculation in the absence of magnetic field and then we included the effect of moderate $B$ values (around 1–2 T) as used in the AEgIS experiment. Previous works concerning charge exchange of antiprotons with Rydberg positronium are limited to collision velocities and magnetic fields higher than that considered here [16] and to a different dynamic regime in which the

*Corresponding author: Gemma.Testera@ge.infn.it

 

initial positronium state is a long-lived delocalized outer well state [17]. Other works [18,19] extend the calculation to low collision velocity but only consider positronium in low excited states ($n_{P_s} = 3$ at maximum). Finally other studies [20,21] are focused on modeling the dynamics of the antihydrogen formation by a double process of charge exchange (as in the ATRAP experiment [15]), the first one producing the Rydberg positronium and the second one producing the antihydrogen.

Our calculations show that, in the absence of magnetic fields, the cross section scaled by $n_{P_s}^4$ has a universal shape as a function of the ratio $k_v$ between the velocity of the center of mass of $P_s^*$ and that of the positron in the positronium classical circular orbit. This universal shape is valid for all the values of $n_{P_s}$ that we have investigated (ranging from 3 to 50). Below about $k_v \simeq 0.3$ the scaled cross section increases as $1/k_v^2$ or, in an equivalent way, as $1/E_{P_s}^{cm}$ being $E_{P_s}^{cm}$ the positronium center-of-mass kinetic energy. This result extends the one reported in Refs. [18,19] limited to $n_{P_s} \leqslant 3$. This low velocity behavior of the charge-exchange process and the high values of the cross section have interesting consequences for the antihydrogen experiments and suggest that the production of a large number of cold antihydrogen needs very cold Rydberg positronium.

The interest of the reaction of antiprotons with cold positronium emerges also from the analysis of the distribution of the principal quantum number of the formed antihydrogen: low velocity collisions (in the $1/E_{P_s}^{cm}$ regime) produce antihydrogen with a narrow distribution of principal quantum numbers which is advantageous for performing on them further atomic manipulations [22]. Higher velocity collisions produce antihydrogen populating a distribution with a large spread of principal quantum numbers.

We included in the calculation the presence of a magnetic field as needed to trap the antiprotons: we found that at very low velocities the cross section no longer increases as $1/k_v^2$ ($1/E_{P_s}^{cm}$) and its universal behavior is broken. This reduction of the cross section depends on the flight direction of the incoming positronium with respect to the magnetic field. Interestingly there is a significant range of collision velocity where the cross section increases in the presence of magnetic field.

We first recall some basic principles of the CTMC method and we show the results obtained in the absence of magnetic field. We then explain how the CTMC method is extended to include the effect of the magnetic field and we show the relevant results.

## II. CLASSICAL TRAJECTORY MONTE CARLO METHOD

In the absence of magnetic field the interaction between $P_s^*$ in the initial quantum state defined by $n_{P_s}, l_{P_s}, m_{P_s}$ with an antiproton may result in the antihydrogen formation [see Eq. (1)] but also in $P_s^*$ elastic or inelastic scattering or ionization as relation (2) shows,

$$\begin{aligned} &P_s^*(n_{P_s}, l_{P_s}, m_{P_s}) + \bar{p} \rightarrow P_s^*(n_{P_s}, l_{P_s}, m_{P_s}) + \bar{p} \\ &P_s^*(n_{P_s}, l_{P_s}, m_{P_s}) + \bar{p} \rightarrow P_s^*(n'_{P_s}, l'_{P_s}, m'_{P_s}) + \bar{p} \quad . \\ &P_s^*(n_{P_s}, l_{P_s}, m_{P_s}) + \bar{p} \rightarrow e^+ + e^- + \bar{p} \end{aligned} \tag{2}$$

The CTMC method was introduced in Ref. [23] to calculate capture and ionization cross sections for proton-hydrogen collisions [24] and it has been extensively used also to model three-body processes [25] and multielectron targets [26]. It is particularly well suited to model processes involving Rydberg atoms and automatically allows us to account for all the mentioned collision channels.

The CTMC procedure is based on solving the classical equation of motion for a three-body, three-dimensional system made of the positron and electron initially bound in the positronium atom and the target antiproton. We solve the classical equation of motion with the Hamiltonian $H_{tot}$ neglecting the spin. Using atomic units, $H_{tot}$ in the absence of external fields is given by

$$H_{tot} = \frac{\pi_{\bar{p}}^2}{2m_{\bar{p}}} + \frac{\pi_{e^+}^2}{2} + \frac{\pi_{e^-}^2}{2} - \frac{1}{r_{e^+e^-}} - \frac{1}{r_{\bar{p}e^+}} + \frac{1}{r_{\bar{p}e^-}}, \tag{3}$$

where $\vec{r}_{\bar{p}}$ and $\vec{\pi}_{\bar{p}} = m_{\bar{p}}\vec{v}_{\bar{p}}$ are the position and the mechanical momentum of the antiproton in the laboratory reference frame, $\vec{r}_{e^+}$, $\vec{\pi}_{e^+}$, $\vec{r}_{e^-}$, and $\vec{\pi}_{e^-}$ are the corresponding quantities for the positron and the electron, and $r_{e^+e^-}, r_{\bar{p}e^+}, r_{\bar{p}e^-}$ are the distances between each couple of particles.

The initial conditions are randomly sampled. For each sorted initial state the classical trajectories are calculated starting from a large separation between antiproton and positronium to a distance of closest approach and out again to a large separation between the antiproton and the electron. The Coulomb force among the three-body is included in all the steps of the simulation. If at the end of each simulation the positron is found to be bound to the antiproton then the reaction is classified as antihydrogen formation. In detail the steps of the CTMC method are as follows:

(i) sampling of the initial conditions;
(ii) integration of the equations of motion;
(iii) identification of the final conditions;
(iv) calculation of the cross section.

### A. Sampling of the initial conditions

Figure 1 shows the geometry of the collision. The antiproton is initially at rest in the position $z = z_{\bar{p}}^i$. The initial position of the center of mass of the $P_s^*$ atom is in the $z = 0$ plane; the impact parameter $b^{Imp}$ is chosen generating its radial position within a circle of radius $b_{max}$. The value of $b_{max}$ may depend on the process in which we are interested (ionization, excitation,

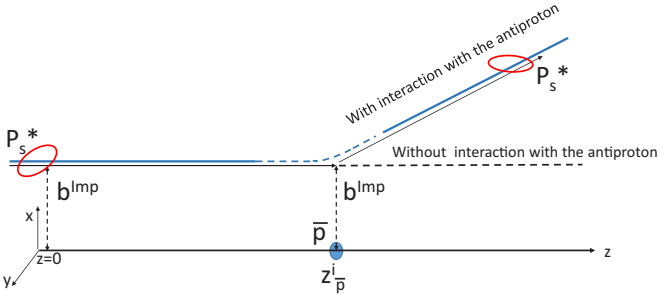


FIG. 1. Definition of the geometry of the collision without magnetic field with a pictorial view of the trajectories of the center of mass of $P_s^*$ with and without interaction with the antiproton. The trajectory of $P_s^*$ in the case of absence of interaction with the antiproton is a straight line along $z$. $b^{Imp}$ is the impact parameter.

charge exchange): it is chosen as the minimum value $b_{\max}$ such that adding trajectories with $b^{\mathrm{Imp}} > b_{\max}$ the resulting variation of the cross section is negligible within the statistical uncertainty of the calculation.

The initial conditions in the phase space describing the positronium must be selected from a statistical distribution of the classical variables that matches the corresponding quantum mechanical distribution. As widely discussed in Refs. [23,27], we adopt the choice of picking up initial conditions from a microcanonical ensemble. This allows matching the quantum-mechanical energy and momentum distributions. The generation of the initial conditions for $\mathrm{P}_s^*$ begins by considering the Hamiltonian of the $e^+$, $e^-$ system and separating the center-of-mass motion from the relative motion of the $e^+$ and $e^-$. The relative motion is that of a particle with reduced mass $\mu = 1/2$ in the Coulomb potential and the classical orbits for the bound system are Kepler elliptical orbits. Energy and angular momentum are conserved.

$\mathrm{P}_s^*$ in the quantum state with principal quantum number $n_{\mathrm{P}_s}$ is then described by generating ellipses corresponding to the energy $E_{n_{\mathrm{P}_s}} = \frac{1}{4n_{\mathrm{P}_s}^2}$. Specifying the energy only defines the semiaxis major $a_{n_{\mathrm{P}_s}}$ ($a_{n_{\mathrm{P}_s}} = 2n_{\mathrm{P}_s}^2$) being the semiaxis minor $b_{nl_{\mathrm{P}_s}}$ related to the classical angular momentum $L_c$. In the microcanonical ensemble [23] the classical squared angular momentum $L_c^2 = (\vec{r} \wedge \vec{\pi})^2$ is uniformly distributed between 0 and its maximum allowed value. For a given $n_{\mathrm{P}_s}$ value we then generated $L_c^2$ with uniform distribution and then the corresponding $b_{nl_{\mathrm{P}_s}}$. The quantal weights are reproduced for all the $l_{\mathrm{P}_s}$ values by defining $l_{\mathrm{P}_s}$ as

$$l_{\mathrm{P}_s} \ll L_c/\hbar \leqslant l_{\mathrm{P}_s} + 1 \tag{4}$$

with $l_{\mathrm{P}_s} = 0,1,\ldots n_{\mathrm{P}_s} - 1$. $b_{nl_{\mathrm{P}_s}}$ is then given by $b_{nl_{\mathrm{P}_s}} = 2n_{\mathrm{P}_s}\sqrt{l_{\mathrm{P}_s}(l_{\mathrm{P}_s}+1)}$.

The starting coordinates and velocities in the ellipse have been generated by solving the motion equation of the selected elliptical trajectory for one period and then picking up a time value with random uniform distribution between 0 and the ellipse period (and the corresponding coordinates and velocities).

The orientation of the ellipse plane is linked to the projection of the angular momentum along the $z$ axis and thus to the $m_{\mathrm{P}_s}$ quantum number. All the $m_{\mathrm{P}_s}$ values are generated by introducing a rotation with three Euler angles.

The velocity of the center of mass of the positronium $\vec{v}_{\mathrm{P}_s}^{\mathrm{cm}}$ defines the collision velocity as we assume that the antiproton is at rest. Of course identical results would be obtained by considering the motion of the antiproton and defining $\vec{v}_{\mathrm{P}_s}^{\mathrm{cm}}$ as the relative velocity (in the laboratory frame) between positronium and antiproton. It is generally known that the processes corresponding to relations 1, 2 involving Rydberg atoms and ions [27] have huge cross sections when the impact speed is close to the mean speed $v_n$ of the Rydberg electron. We thus define the parameter $k_v$ as the ratio between $v_{\mathrm{P}_s}^{\mathrm{cm}}$ and the velocity of the positron $\frac{1}{2n_{\mathrm{P}_s}}$ in the $\mathrm{P}_s^*$ center of mass in the circular orbit,

$$k_v = \frac{v_{\mathrm{P}_s}^{\mathrm{cm}}}{2n_{\mathrm{P}_s}}. \tag{5}$$

We assumed that $\vec{v}_{\mathrm{P}_s}^{\mathrm{cm}}$ is along the $z$ direction.

### B. Integration of the equations of motion

We used a six-order Runge-Kutta method with a variable time interval. We calculated at each step $\mathrm{H}_{\mathrm{tot}}$ and we used the difference $\mathrm{H}_{\mathrm{diff}}$ between the actual value of $\mathrm{H}_{\mathrm{tot}}$ and its initial value as a check of the accuracy of the calculation. Typically $|\mathrm{H}_{\mathrm{diff}}/\mathrm{H}_{\mathrm{tot}}| \simeq 10^{-7}$. Trajectories that do not conserve the energy were discarded. They are less than 0.05% of the total.

We selected $z_{\bar{p}}^i$ (see Fig. 1) and the distance between the antiproton and the electron where the simulation should be stopped three times larger than the maximum impact parameter. We have checked the stability of the results with respect to these choices.

### C. Identification of the final conditions

The classification of the final state is performed analyzing the Hamiltonian $\mathrm{H}_{e^+e^-}$, $\mathrm{H}_{\bar{p}e^+}$ of the relative motion between couples of particles,

$$\mathrm{H}_{e^+e^-} = \pi_{e^+e^-}^2 - \frac{1}{r_{e^+e^-}}, \tag{6}$$

where $\pi_{e^+e^-} = \pi_{e^-} - \pi_{e^+}$ is the mechanical momentum of the relative motion of the couple $e^+e^-$,

$$\mathrm{H}_{\bar{p}e^+} = \frac{\pi_{\bar{p}e^+}^2}{2m_{\bar{p}}} - \frac{1}{r_{\bar{p}e^+}} \tag{7}$$

and $\pi_{\bar{p}e^+} = \pi_{e^+} - \pi_{\bar{p}}$

If at the end of the collision $\mathrm{H}_{e^+e^-} < 0$ and $\mathrm{H}_{\bar{p}e^+} > 0$ then the electron and positron are still bound into the positronium. The principal quantum number $n'_{\mathrm{P}_s}$ is defined according to the value of $\mathrm{H}_{e^+e^-}$ and the comparison between $n_{\mathrm{P}_s}$ and $n'_{\mathrm{P}_s}$ establishes if the collision is elastic or inelastic. If $\mathrm{H}_{e^+e^-} > 0$ and $\mathrm{H}_{\bar{p}e^+} > 0$ then positronium is ionized. Finally if $\mathrm{H}_{e^+e^-} > 0$ and $\mathrm{H}_{\bar{p}e^+} < 0$ the positron is bound to the antiproton, the collision is classified as antihydrogen formation, and its quantum numbers are evaluated.

### D. Calculation of the cross section

The cross section in SI units for charge exchange $\sigma$ and its standard (rms) error $\Delta\sigma$ are obtained using [23]

$$\sigma = \pi a_0^2 b_{\max}^2 \frac{N_{\bar{\mathrm{H}}}}{N_{\mathrm{tot}}}, \tag{8}$$

$$\Delta\sigma = \sigma\sqrt{\frac{N_{\mathrm{tot}} - N_{\bar{\mathrm{H}}}}{N_{\mathrm{tot}} N_{\bar{\mathrm{H}}}}}, \tag{9}$$

where $b_{\max}$ is the maximum value of the impact parameter in atomic units; $N_{\bar{\mathrm{H}}}$ is the number of trajectories resulting in antihydrogen formation and $N_{\mathrm{tot}}$ is the total number of generated trajectories.

The statistical uncertainty of each point in the cross-section plots shown along this paper is often hidden within the size of the plot markers. Typically we run a number of trajectories sufficient to calculate the cross section with a statistical error of 2–3% in the absence of a magnetic field. In presence of a magnetic field, the computation time being longer, in some cases the statistical accuracy is smaller as it appears in the plots. The number of trajectories to be generated depends on the parameters of the collision and it is typically of the order of several tens of thousand.

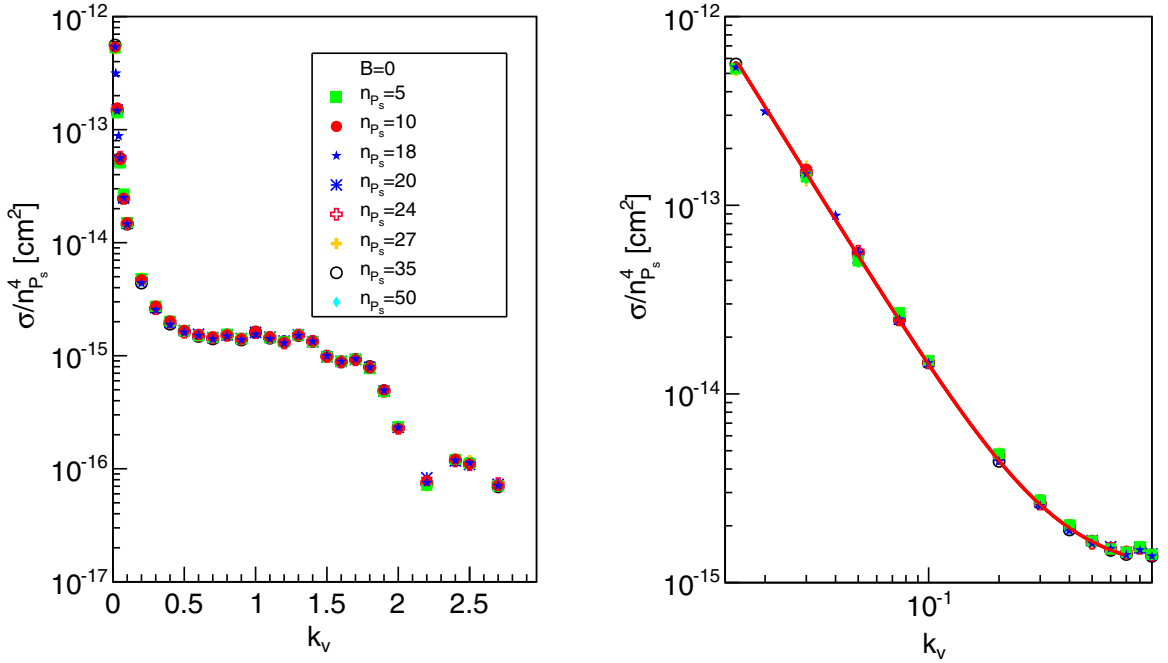


FIG. 2. Charge-exchange cross section divided by $n_{\mathrm{P}_s}^4$ ($\sigma/n_{\mathrm{P}_s}^4$) as a function of $k_v$ with $B = 0$. The results obtained for the various principal quantum numbers shown in the legend collapse into a universal curve and they cannot be distinguished in the plot. For each $n_{\mathrm{P}_s}$ the $l_{\mathrm{P}_s}$ and $m_{\mathrm{P}_s}$ values are sampled from a canonical ensemble as described in Sec. II. The right plot is a zoom of the region with low $k_v$ values with the fit $\sigma/n_{\mathrm{P}_s}^4(\mathrm{cm}^2) = \frac{s_1}{k_v^2} + s_2$ superimposed (red line). $s_1 = 1.32 \times 10^{-16}$ cm$^2$, $s_2 = 1.12 \times 10^{-15}$ cm$^2$.

## III. CHARGE EXCHANGE CROSS SECTION IN ABSENCE OF MAGNETIC FIELD

We first considered positronium in a initial state with $n_{\mathrm{P}_s}$ defined and with all possible values of $l_{\mathrm{P}_s}$ and $m_{\mathrm{P}_s}$ (distributed as described in Sec. II A) and we studied the charge-exchange process as a function of the $\mathrm{P}_s$ center-of-mass velocity through the parameter $k_v$ defined in Eq. (5). We are mostly interested in the values of $n_{\mathrm{P}_s}$ in the interval 13–20, however we performed the calculation for $n_{\mathrm{P}_s}$ spanning the range from 3 to 50.

As anticipated in the Introduction, it turns out that over the whole range of $n_{\mathrm{P}_s}$ values that we have investigated the cross section scales as $n_{\mathrm{P}_s}^4$ and $\sigma/n_{\mathrm{P}_s}^4$ shows a universal behavior as a function of $k_v$ as Fig. 2 shows.

For $k_v \gtrsim 2$–3 the scaled cross section $\sigma/n_{\mathrm{P}_s}^4$ rapidly drops while $k_v \simeq 0.3$ is a threshold below which it rises as $\frac{1}{k_v^2}$ and it reaches interestingly high values. The right plot of Fig. 2 shows the region of low $k_v$ values and a fit with the function $\sigma/n_{\mathrm{P}_s}^4(\mathrm{cm}^2) = \frac{s_1}{k_v^2} + s_2$.

The same points plotted as a function of the center-of-mass energy of positronium $E_{\mathrm{P}_s}^{\mathrm{cm}}$ are shown in Fig. 3. The $\frac{1}{k_v^2}$ law of course translates to an increase of the cross section as $1/E_{\mathrm{P}_s}^{\mathrm{cm}}$. This trend was previously found using the two-center convergent close-couplng (CCC) method for $n_{\mathrm{P}_s} = 2,3$ [18,19] and here we show that it is obtained for collisions involving Rydberg positronium and antiprotons. The onset of the $1/E_{\mathrm{P}_s}^{\mathrm{cm}}$ regime approximately scales as $1/n_{\mathrm{P}_s}$.

The rise of the cross section in the case of low-energy Rydberg positronium and its high values are two results of extreme interest for the design and the optimization of the antihydrogen experiments.

Generally for a fixed value of $n_{\mathrm{P}_s}$ the cross section depends on the initial angular state of the positronium: this is exemplified in Fig. 4 for $n_{\mathrm{P}_s} = 18$. Particularly the differences

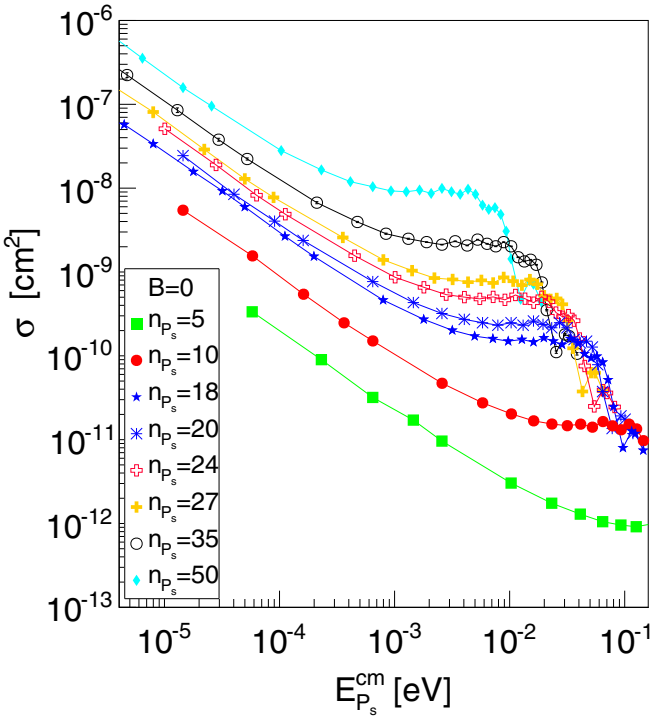


FIG. 3. Charge-exchange cross section $\sigma$ as a function of the $\mathrm{P}_s$ center-of-mass energy. The plot shows the same points of Fig. 2. The lines simply connect the points to help the graphical interpretation.

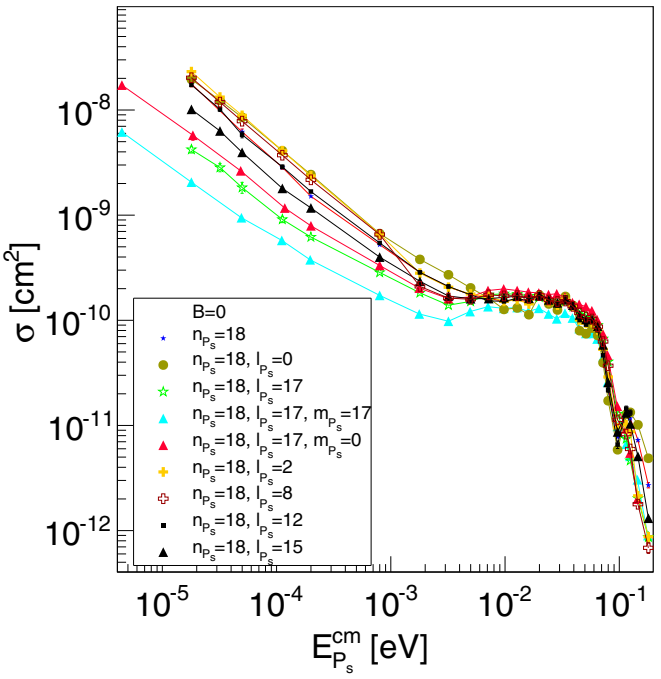


FIG. 4. Charge-exchange cross section as a function of the $P_s$ center-of-mass energy for $n_{P_s} = 18$ and various values of the angular momentum quantum numbers. The plot with $l_{P_s}$ or $m_{P_s}$ not specified has been obtained with a statistical distribution of angular momenta. The lines simply connect the points to help the graphical interpretation.

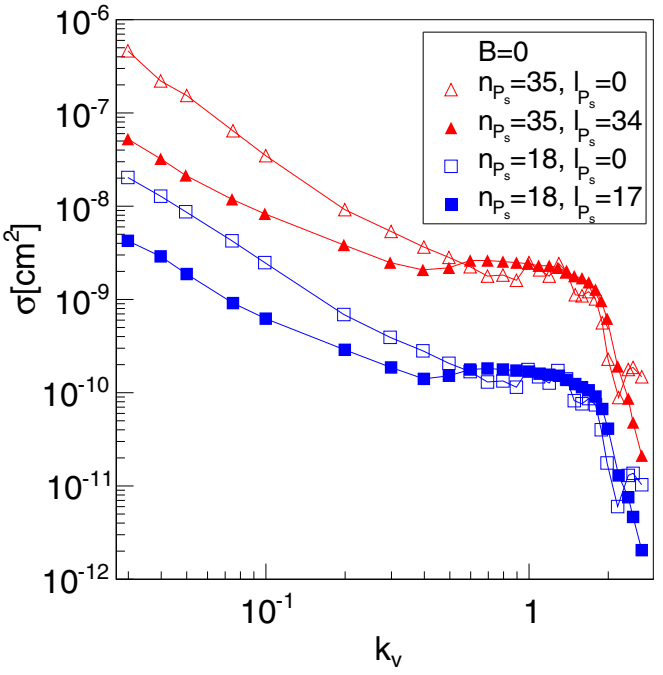


FIG. 5. Charge-exchange cross section for positronium in the initial state with $n_{P_s} = 18$ and 35 and with the extreme values of the angular momentum quantum number ($l_{P_s} = 0$ and $l_{P_s} = n_{P_s} - 1$) as a function of $k_v$. The lines simply connect the points to help the graphical interpretation.

are enhanced in the low-energy region ($1/E^{cm}_{P_s}$ regime) being the charge-exchange probability significantly higher for the lowest angular momentum states than for the highest ones. This general tendency is reproduced for other values of $n_{P_s}$. Figure 5 shows the cross section as a function of the reduced velocity $k_v$ for $n_{P_s} = 18$ and $n_{P_s} = 35$ and the extreme values of the angular momentum ($l_{P_s} = 0$ and $l_{P_s} = n_{P_s} - 1$). The $k_v$ threshold below which the cross section approximately scales as $E^{-1}_{P_s}$ is about 0.9 for $l = 0$ and about 0.4 for $l = n - 1$. We have also investigated for $l_{P_s} = n_{P_s} - 1$ the role of $m_{P_s}$ and found that in the low-energy region there is also a dependence of the cross section upon $m_{P_s}$ with high $m_{P_s}$ giving a lower cross section. Examples are in Fig. 4.

Our results are in perfect agreement with the CTMC calculation reported in Ref. [16] for $n_{P_s} = 50$ and limited to $k_v > 0.5$.

The accuracy of the classical CTMC is expected to increase with the values of the principal quantum number of $P_s$ but the limits of the validity of the classical approach are unclear. The comparison between the low velocity cross section obtained with the CTMC and the result of the CCC method described in Refs. [18,19] for collisions involving $n_{P_s} = 3$ and $l_{P_s} = 0$ or $n_{P_s} = 3$ and a statistical distribution of $l_{P_s}$ is reported in Fig. 6. The two methods show the same shape of the cross section as a function of the collision velocity with discrepancies in the numerical values of a few ten %.

The CTMC and CCC methods also agree in describing the qualitative proportion of the $\bar{H}$ final-state distribution with $n_{P_s} = 3$ in the $1/E^{cm}_{P_s}$ regime: the dominant channel in the one originating $\bar{H}$ with $n = 4$ followed by that giving $n = 3$ with the production of antihydrogen with $n = 1$ and 2 accounting only for a few percent or less of the total. However, as an example, in case of collisions induced by $n_{P_s} = 3$ and $l_{P_s} = 0$, the ratio between the cross section for producing $n_{\bar{H}} = 4$ and

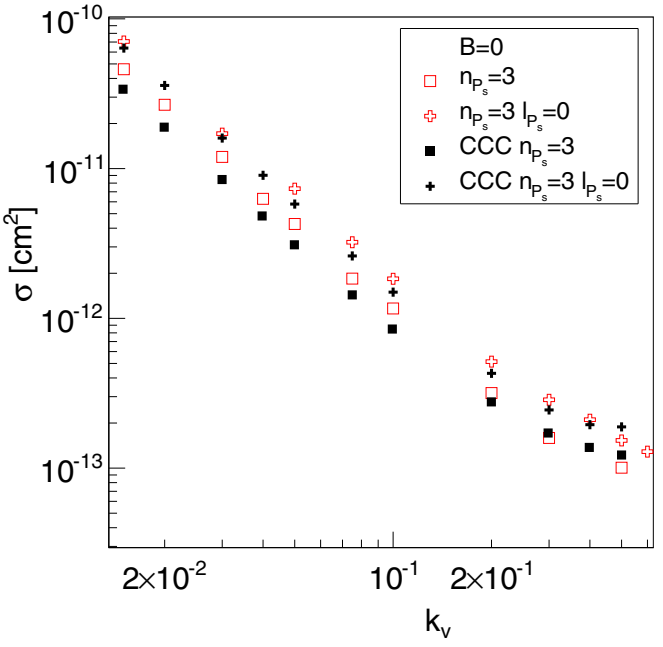


FIG. 6. Low-energy charge-exchange cross section calculated with our CTMC method (open red squares and open red crosses) and with the CCC method (filled black squares and filled black crosses) of [18,19].

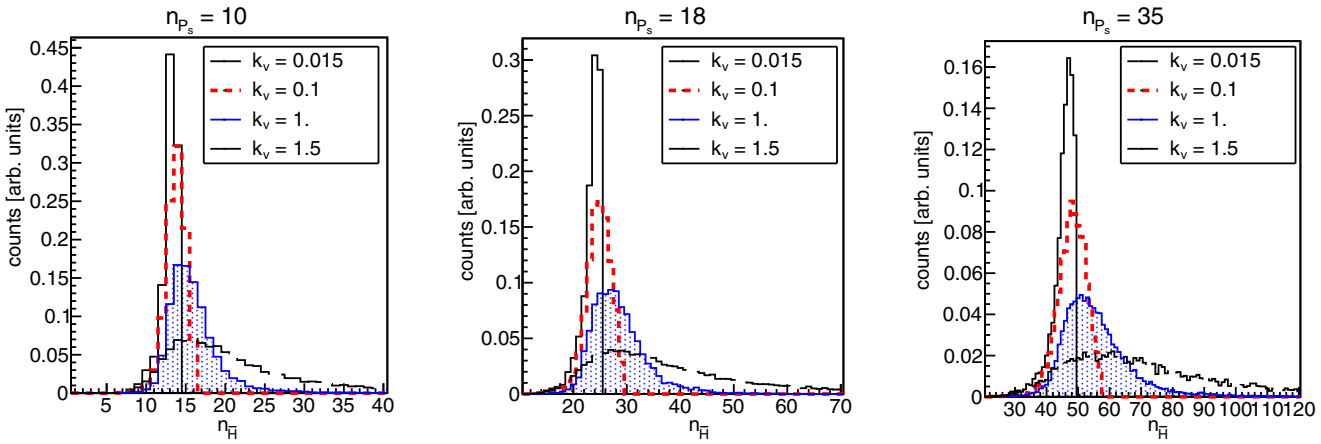


FIG. 7. Normalized distribution of the principal quantum number of antihydrogen produced by interaction with $P_s$ with $n_{P_s} = 10$, 18, 35, and all the values of $l_{P_s}$ and $m_{P_s}$. $B = 0$.

$n_{\bar{H}} = 3$ is close to 20 in CCC while it is slightly higher than 10 in the CTMC approach.

### A. Distribution of the antihydrogen quantum numbers

Our CTMC model shows that the antihydrogen atoms are always formed with a distribution of the principal quantum number $n_{\mathrm{Hbar}}$ even when the incoming $P_s^*$ has a fixed $n_{P_s}$. The distribution is roughly peaked around $n_0 = \sqrt{2} n_{P_s}$ corresponding to the same binding energy of the positron in the initial positronium and in the final antihydrogen. From standard kinematic arguments it follows that the antihydrogen formation in the limit of both positronium and antiproton at rest can only happen if the $Q$ value of the reaction, that is the difference of the binding energy of the initial positronium and the final antihydrogen, is positive,

$$Q = \frac{1}{4n_{P_s}^2} - \frac{1}{2n_{\bar{H}}^2}. \tag{10}$$

The condition $Q > 0$ translates into $n_{\bar{H}} \leqslant \sqrt{2} n_{P_s}$. The results of the CTMC consistently show that in the low velocity regime, corresponding to the $1/E_{P_s}^{\mathrm{cm}}$ scaling, the distribution of the principal quantum number of the formed antihydrogen has a small spread, is asymmetric, peaked around $n_0$ with a population of antihydrogen with $n_{\bar{H}} > n_0$ negligible. The CTMC also shows that when $k_v$ is in the range (0.3,1) $n_{\mathrm{Hbar}}$ are produced with a bell-shaped distribution peaked at $n_0$ and with a full width at half maximum $\simeq 0.3 n_0$. For larger values of $k_v$ the produced antihydrogen has a wider distribution of principal quantum numbers with tails extending up to several $n_0$. Figure 7 shows an example of the above-mentioned effect for $n_{P_s} = 10, 18, 35$. The shape of the distribution is practically independent upon $n_{P_s}$ when plotted as a function of $\frac{n_{\bar{H}}}{n_0}$.

### B. Angular momentum of the antihydrogen atoms

Antihydrogen atoms are always produced with a wide distribution of angular momenta $l_{\bar{H}}$ and for each of them all the states with all possible values of $m_{\bar{H}}$ are statistically populated. The shape of the distribution of $l_{\bar{H}}$ shows features that depend on $k_v$ and also on the initial $l_{P_s}$. An example of the above effect is shown in Fig. 8, where antihydrogen formation is studied for $n_{P_s} = 18$ for extremal values of $l_{P_s}$. In both cases in the low velocity regime $k_v < 0.2$ antihydrogen is produced with an angular momentum distribution that does not rise significantly as a function of $l_{\bar{H}}$, while for increasing values of $k_v$ high values of angular momentum become more probable. Note that in the case of equal probability for each angular momentum the $l_{\bar{H}}$ distribution should show a linear shape.

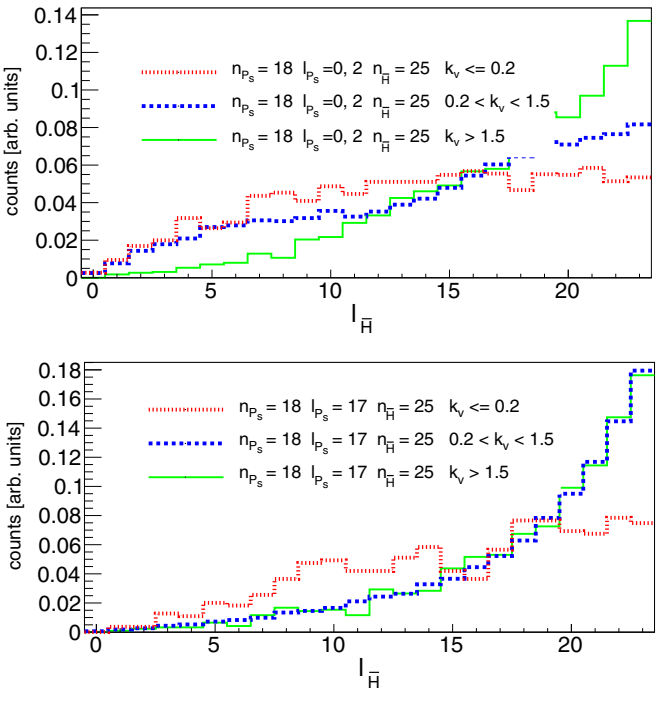


FIG. 8. Distributions (normalized to unit area) of $l_{\bar{H}}$ obtained by collisions with positronium in selected states of angular momentum $l_{P_s}$. The top panel refers to $l_{P_s} = 0$ and $l_{P_s} = 2$ and the bottom one to $l_{P_s} = 17$. The three curves show results obtained selecting different intervals of the $k_v$ parameter as shown in the legend. $k_v < 0.2$ is roughly the onset of the $\frac{1}{E_{P_s}^{\mathrm{cm}}}$ regime.

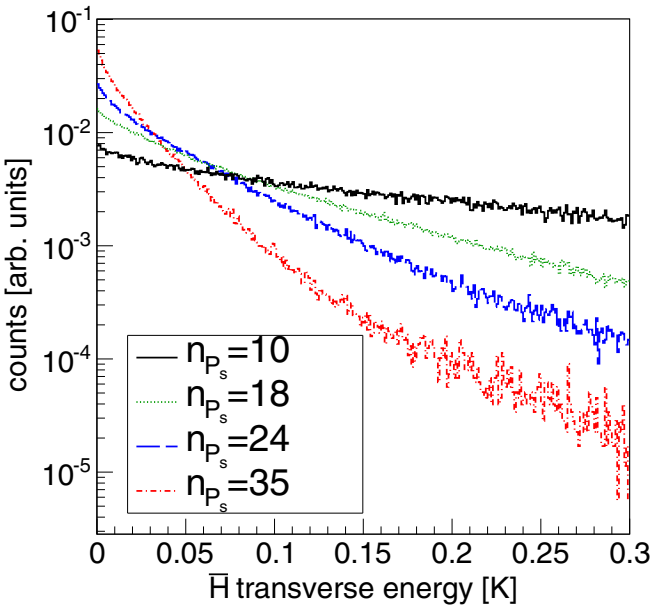


FIG. 9. Distributions (normalized to unit area) of the recoil kinetic energy of the antihydrogen in the direction transverse to $z$ for four different values of $n_{P_s}$. The energy is expressed in K using the relation $\frac{1}{2}m_{\bar{H}}(v_{\bar{H}x}^2 + v_{\bar{H}y}^2) = KT$, with $v_{\bar{H}x}$, $v_{\bar{H}y}$ being the velocities of antihydrogen in the direction perpendicular to $z$. The interaction of antiprotons with high Rydberg states of $P_s$ produces colder antihydrogen. $B = 0$.

### C. Velocity of the antihydrogen

As discussed in the Introduction, the velocity of the antihydrogen is an important parameter that influences the possibility to perform precision experiments. Here we are assuming that the antiproton is initially at rest. If this condition is not fulfilled the recoil velocity here calculated has to be properly added to the initial antiproton velocity.

The recoil velocity of the antihydrogen in the direction perpendicular to the flight direction of the positronium (assumed as $z$) has a null mean value and a spread that decreases while $n_{P_s}$ increases. For a fixed $n_{P_s}$ it does not significantly depend on $k_v$. The fraction of antihydrogen with low radial recoil energy produced by interaction of antiprotons with fixed $n_{P_s}$ positronium increases with $n_{P_s}$ as Fig. 9 shows thus indicating that high Rydberg states of positronium are preferred if one aims to cold antihydrogen.

The antihydrogen gets a small boost (as reported in Fig. 10) along the flight direction of the incoming positronium related to its center-of-mass velocity. This effect is particularly interesting if one is aiming to form a beam of cold antihydrogen and it is required that positronium fly toward the antiprotons along the wished beam direction. However it should be observed that the antihydrogen boost is significant only when $k_v$ is above the $1/k_v^2$ regime and then a proper tradeoff between flux of produced antihydrogen and its directionality has to be practically considered.

### D. Impact parameter

The distributions of the impact parameter of the collisions resulting in antihydrogen formation is shown in Fig. 11. The impact parameter is normalized to the size of the semiaxis

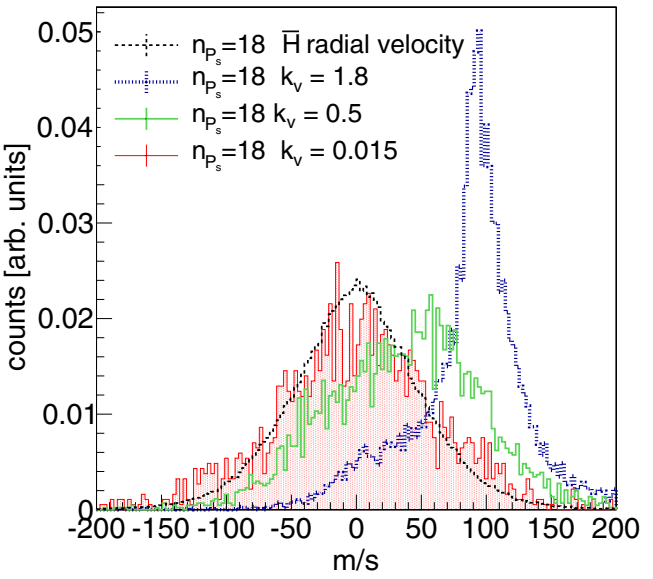


FIG. 10. Distribution of the velocity of the antihydrogen in the flight direction of the positronium ($z$) obtained with $n_{P_s} = 18$ and some selected values of $k_v$. For comparison the distribution of the velocity in one of the transverse directions is reported. All the histograms are normalized to unit area. $B = 0$.

major of the positronium orbit and the distributions are normalized to the unit area. The shape of these scaled distributions is basically the same for all the values of the $n_{P_s}$ investigated. Not surprisingly, large impact parameters allow antihydrogen production only for low velocity collisions thanks to the relatively long time spent by the positronium in the proximity of the antiproton.

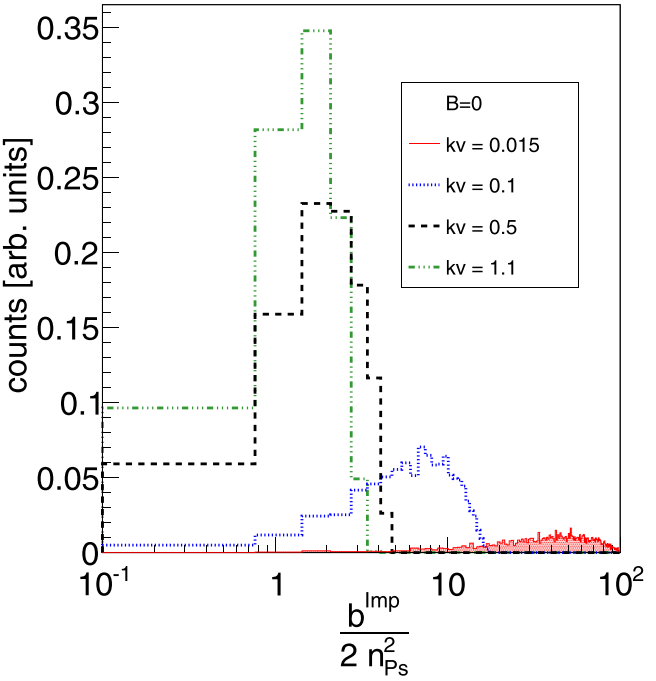


FIG. 11. Distributions (normalized to unit area) of the impact parameters (scaled by the positronium orbit semiaxis major) of the collisions resulting in antihydrogen formation. $B = 0$.

## IV. CHARGE EXCHANGE IN PRESENCE OF MAGNETIC FIELD

### A. Coupling between center of mass and internal motion

We have extended the CTMC approach including the presence of an external magnetic field $\vec{B}$. We consider here fields of moderate values ($B \simeq 0.5$–$2$ T) as foreseen in the AEgIS experiment [2].

The magnetic field influences the dynamics of the collision and the initial and final status of $P_s^*$ and $\bar{H}$. Particularly important is the fact that the Hamiltonian of a two-body charged system in magnetic field cannot be separated as the sum of two contributions, one describing the center of mass and the other one the internal motion as in the free field case. This result applies both to the description of positronium and antihydrogen; nevertheless the separation is a good approximation only in the limit of infinite mass of one of two particles. We do not then discuss this coupling between degrees of freedom for antihydrogen while we fully take it into account for positronium. The Hamiltonian of $P_s$ in the presence of magnetic field is

$$H = \frac{1}{2}[\vec{p}_{e^+} + \vec{A}(\vec{r}_{e^+})]^2 + \frac{1}{2}[\vec{p}_{e^-} - \vec{A}(\vec{r}_{e^-})]^2 - \frac{1}{r_{e^+e^-}}, \quad (11)$$

where the canonical momentum $\vec{p}_{e^+}$ is related to the mechanical momentum $\vec{\pi}_{e^+}$ through the usual relation $\vec{\pi}_{e^+} = \vec{p}_{e^+} - \vec{A}(\vec{r}_{e^+})$ and $\vec{\pi}_{e^-} = \vec{p}_{e^-} + \vec{A}(\vec{r}_{e^-})$. $\vec{A}(\vec{r}_{e^+,e^-}) = \frac{1}{2}\vec{B} \wedge \vec{r}_{e^+,e^-}$ is the vector potential.

It is useful to introduce the pseudomomentum [28] of the positron $\vec{k}_{e^+} = \vec{p}_{e^+} - \frac{1}{2}\vec{B} \wedge \vec{r}_{e^+}$ and of the electron $\vec{k}_{e^-} = \vec{p}_{e^-} + \frac{1}{2}\vec{B} \wedge \vec{r}_{e^-}$. In the absence of magnetic field the total mechanical momentum is conserved but in the presence of magnetic field the total canonical momentum $\vec{P}_{P_s} = \vec{p}_{e_+} + \vec{p}_{e_-}$ does not commute with the Hamiltonian and it is not conserved. However the total pseudomomentum $\vec{K}_{P_s}$ is conserved,

$$\vec{K}_{P_s} = \vec{k}_{e^+} + \vec{k}_{e^-} = \vec{P}_{P_s} + \frac{1}{2}\vec{B} \wedge (\vec{r}_{e^-} - \vec{r}_{e^+}). \quad (12)$$

Using the center-of-mass coordinate $\vec{R}_{P_s}$ and pseudomomentum $\vec{K}_{P_s}$ as one set of canonically conjugated variables and the relative coordinates and momentum $\vec{r}_{e^+e^-}$ and $\vec{p}_{e^+e^-}$ as a second set the Hamiltonian becomes

$$H = \frac{K_{P_s}^2}{4} - \frac{1}{2}(\vec{K}_{P_s} \wedge \vec{B}) \cdot \vec{r}_{e^+e^-} + p_{e^+e^-}^2 + \frac{1}{4}(\vec{B} \wedge \vec{r}_{e^+e^-})^2 - \frac{1}{r_{e^+e^-}} \quad (13)$$

and the motion equations are then written in a form that clearly shows the coupling between internal and center-of-mass degrees of freedom [29,30],

$$\begin{aligned} \frac{d\vec{R}_{P_s}}{dt} &= \frac{1}{2}\vec{K}_{P_s} - \frac{1}{2}(\vec{B} \wedge \vec{r}_{e^+e^-}) \\ \frac{d\vec{K}_{P_s}}{dt} &= 0 \quad \frac{d\vec{r}_{e^+e^-}}{dt} = 2\vec{p}_{e^+e^-} \\ \frac{d\vec{p}_{e^+e^-}}{dt} &= -\frac{1}{2}(\vec{B} \wedge \vec{K}_{P_s}) + \frac{1}{2}\vec{B} \wedge (\vec{B} \wedge \vec{r}_{e^+e^-}) - \frac{\vec{r}_{e^+e^-}}{r_{e^+e^-}^3}. \end{aligned} \quad (14)$$

One of the consequences of the internal and center-of-mass motion coupling is that the center of mass does not move on straight line trajectory as in the field-free case. The center-of-mass trajectory is related to the time-dependent relative coordinate $\vec{r}_{e^+e^-}$ while the internal motion depends on the center of mass through the conserved quantity $\vec{K}_{P_s}$. These features have been discussed in Refs. [29–31] where it is also underlined that the dynamics is not determined by the energy $E$ and magnetic-field strength separately but only on the scaled quantity $\epsilon = EB^{-2/3}$. Varying $\epsilon$ from $-3$ to $-0.1$ the internal motion undergoes a transition from regular motion to chaos. With the magnetic fields and energies here considered we expect to be in the fully regular regime.

### B. Construction of classical trajectories corresponding to quantum states of $P_s^*$ in magnetic field

We employed the adiabatic switching procedure [32] to construct trajectories corresponding to quantum states of Rydberg $P_s$ in magnetic field. This method is largely used for nonseparable systems [33] and it has been recently suggested for the description of quantum states of hydrogen in magnetic field [34]. An alternative approach is based on the modification of the classical elliptical trajectories in the presence of magnetic field as reported [35]. This method, introduced for Rydberg atoms, is not appropriate for Rydberg $P_s$ because it does not consider the coupling between center of mass and internal motion. The adiabatic switching procedure automatically takes into account this coupling and produces a final state in which the center of mass and the internal degrees of freedom are coherently described.

We randomly selected elliptical trajectories of $P_s^*$ in the absence of magnetic field as described in Sec. II A and we then followed the full motion (center of mass and internal motion) of $P_s^*$ while the external magnetic field is adiabatically switched on. In practice we solved the motion equation for the Hamiltonian $H(t)$ [as in relations (11) and (13)] with the addition of a time-dependent magnetic field $\vec{B}^{\text{adiab}}(t) = \lambda(t)\vec{B}$ slowly rising from 0 to the final value $\vec{B}$. We tuned $\lambda(t)$ in such a way that the full field is reached after some thousands of periods of the unperturbed elliptical motion $\tau_n = 4\pi n_{P_s}^3$. We have checked that the results about the cross section are stable as a function of the time used to ramp the magnetic field.

Sampling the initial state from a microcanonical ensemble simply ensures that all possible initial states are considered. Note that neither the angular momentum nor its $z$ component are conserved in general conditions with not null $K_{P_s}$.

The conservation of $\vec{K}_{P_s}$ leads to the conservation of the component of the center-of-mass velocity of $P_s$ in the direction of the magnetic field. Instead the components transverse to the field are not conserved and, as result of the coupling between center of mass and internal motion, at the end of the adiabatic switching of the magnetic field we obtain a center-of-mass velocity in the direction transverse to the magnetic field despite its eventually null initial value. The trajectories of the center of mass of Rydberg $P_s$ in magnetic field are then characterized by significant excursions in the plane perpendicular to $\vec{B}$ and they show substantial deviations from the field-free straight lines. Figure 12 refers to $n_{P_s} = 18$, $B = 1$ T directed along $z$ and it shows some arbitrary example of center-of-mass trajectories

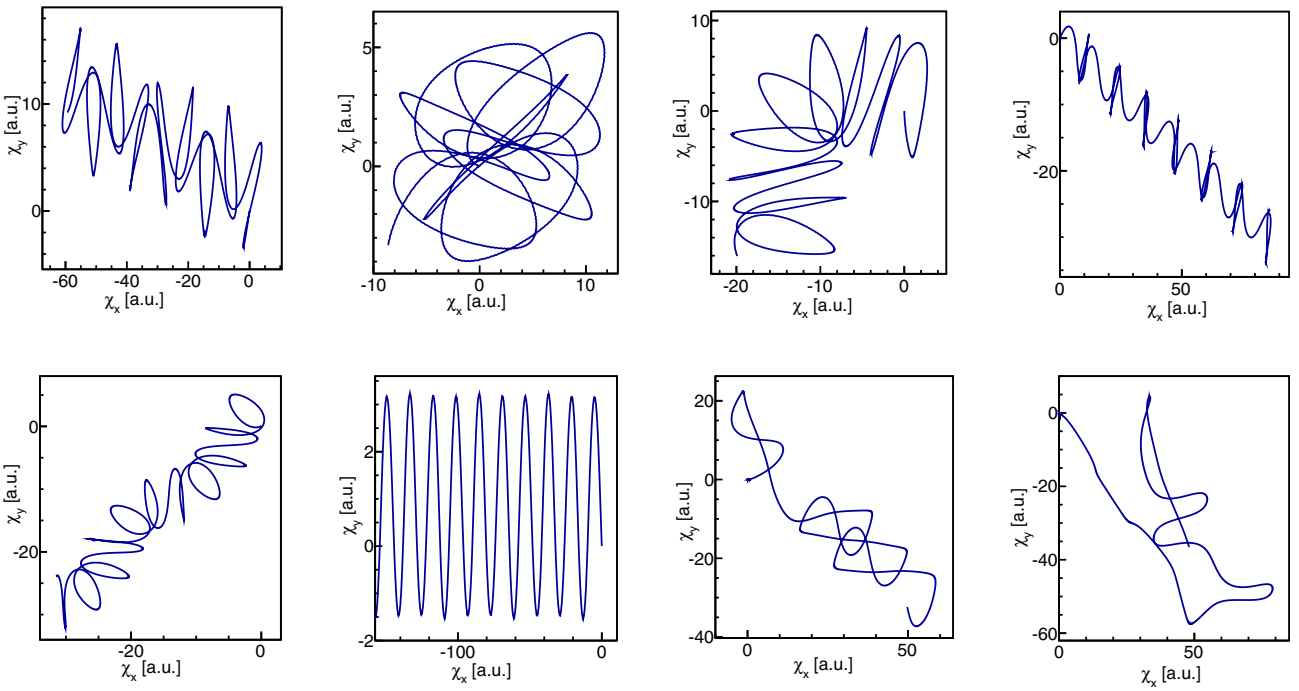


FIG. 12. Example of projection in the $xy$ plane of some trajectories of the center of mass of $P_s$ with $n_{P_s} = 18$ flying in 1-T magnetic field directed along $z$ for a time interval of $5000\tau_n$ following the adiabatic switching of the magnetic field. These trajectories have been calculated without interaction with the antiproton. The $P_s$ center of mass is placed in ($x = 0$, $y = 0$, $z = 0$) at the end of the adiabatic switching of $\vec{B}$. A random elliptical trajectory is initially selected as discussed in Sec. II A and the adiabatic switching procedure is then performed raising the magnetic field in $1000\tau_n$. The shape of this $xy$ projection does not depend on the conserved $z$ velocity of the $P_s$ center of mass. We plot the quantity $\chi_x = x^{\rm cm}_{P_s}/(2n^2_{P_s})$ and $\chi_y = y^{\rm cm}_{P_s}/(2n^2_{P_s})$, that is, the transverse coordinates scaled by the size of the semiaxis major of the unperturbed elliptical trajectory of $P_s$.

of $P_s^*$ projected in the $x$-$y$ plane. They have been obtained tracking the $P_s^*$ motion without interaction with antiproton for a time interval of $5000\tau_n$ after the adiabatic switching of the magnetic field.

Discussions about the center-of-mass trajectories in the case of $\vec{K}_{P_s} = 0$ can be found in Ref. [29]; we did not attempt here to perform a classification or a general study of the features of these trajectories in the general case of a not null $\vec{K}_{P_s}$.

The internal motion is still described within good approximation by elliptical trajectories with not constant semiaxis minor (corresponding to a not conserved angular momentum) and with not constant orientation in space (corresponding to a not conserved projection of the angular momentum in the direction of the magnetic field). For particular values of $K_{P_s}$ and $B$ one would expect the existence of long-lived delocalized states of positronium as a minimum of the potential could appear in addition to the Coulomb singularity at null interparticle distance. These states are predicted to appear when the transverse pseudomomentum is above a critical value $K_c$ with $K_c = (27B/2)^{1/3}$ [17]. These delocalized states are the initial states in the calculation of the charge-exchange cross section in magnetic field in Ref. [16] but they do not play a role here.

In order to fully randomize the $P_s^*$ initial conditions to be used in the charge-exchange process, after the completion of the adiabatic switching of the magnetic field, we followed the motion of $P_s^*$ without interaction with the antiproton for a random time interval of a few thousand $\tau_n$. We used the center-of-mass velocity and the position and velocity of the internal motion obtained at the end of this randomization procedure as initial values of the full three-body tracking in magnetic field with interaction with the antiproton. The choice of the initial position of the center of mass of $P_s^*$ is discussed in Sec. IV C.

Figure 13 shows an example of the distributions of the center-of-mass velocity along the $x$ direction obtained at the end of the adiabatic switching and randomization procedures with $\vec{B}$ along $z$. A similar shape is obtained for the $y$ component. Note that, depending on the $k_v$ value, the transverse center-of-mass velocity acquired by the $P_s^*$ can be a small fraction of the axial one or it can be even larger than that. In any case, the non-null radial velocity of the center of mass has the consequence that $P_s^*$ is emerging from a given position with an angle $\theta_{P_s}$ with respect to the $z$ axis. Figure 14 shows some distributions of this angle in the case of $n_{P_s} = 18$ and $B_z = 1$ T.

### C. Impact parameter for collisions in presence of magnetic field

The definition of cross section and impact parameter in the presence of magnetic field deserves some caveats related to the curved trajectories of the $P_s^*$ center of mass in the absence of interaction with the antiproton. Figure 1 shows the standard definition of the impact parameter $b^{\rm Imp}$: it is the distance that would be the distance of closest approach between the projectile ($P_s^*$) and the target ($\bar{p}$) in the absence of interaction under the assumption that the unperturbed trajectory of the

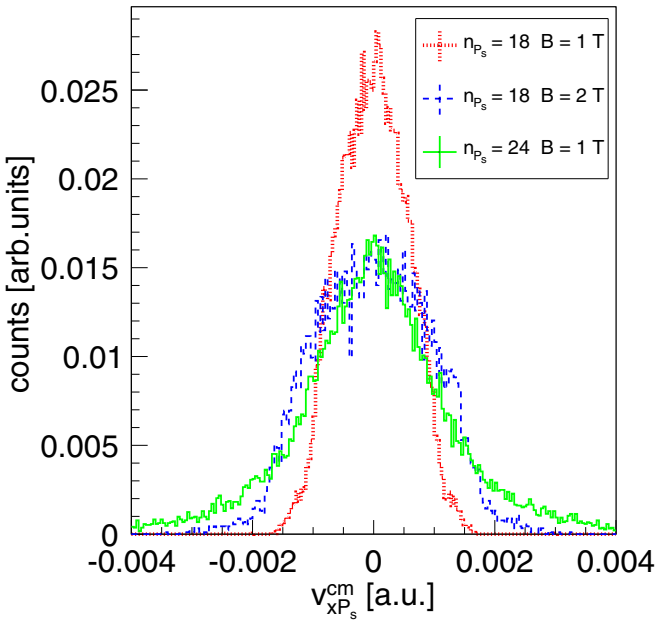


FIG. 13. Example of distributions (normalized to unit area) of one component of the $P_s$ center-of-mass transverse velocity obtained after the adiabatic switching and randomization procedure with $\vec{B}$ along the $z$ axis. The initial transverse velocity is null.

projectile would be a straight line [36]. In an equivalent way we can draw a line parallel to the unperturbed projectile trajectory and passing through the target center (this is the $z$ axis in all this work) and see that $b^{\rm Imp}$ is the distance between these two parallel lines.

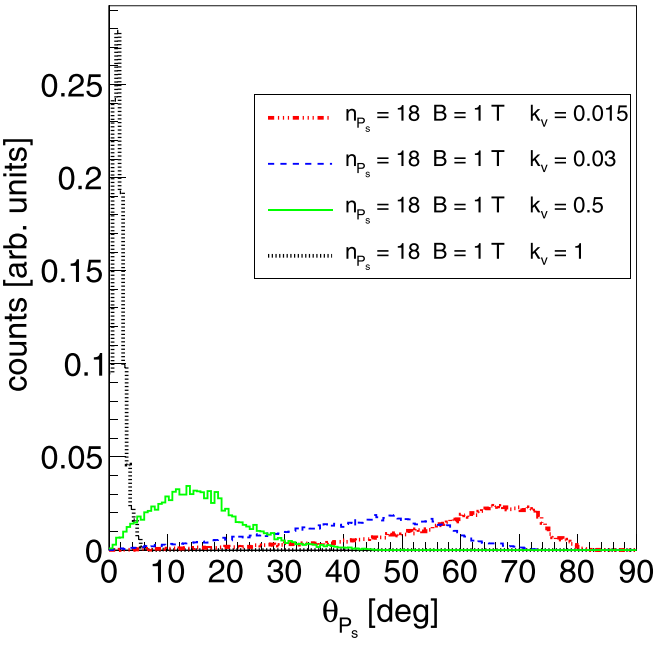


FIG. 14. Distributions (normalized to unit area) of the angle $\theta_{P_s}$ between the axial and transverse center-of-mass velocity of $P_s$ obtained after the adiabatic switching and randomization procedure with $B = 1$ T and $n_{P_s} = 18$.

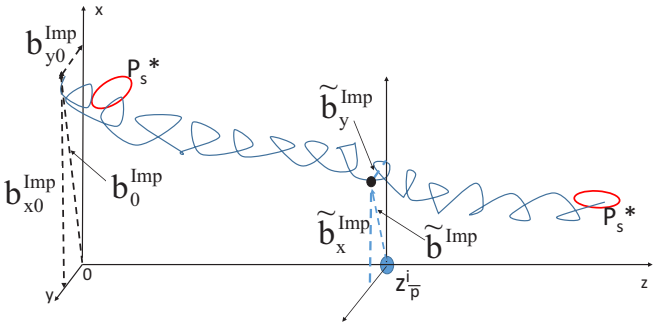


FIG. 15. Definition of the geometry of the collision in presence of magnetic field. The curve shows a pictorial view of a trajectory of the $P_s^*$ center-of-mass trajectory without interaction with the antiproton. The impact parameter used for the calculation of the cross section in presence of magnetic field is $\tilde{b}^{\rm Imp}$ and it represents the distance between the $P_s^*$ trajectory and the point $z^i_{\bar{p}}$ evaluated in the plane $z = z^i_{\bar{p}}$. $\tilde{b}^{\rm Imp} = \sqrt{(\tilde{b}^{\rm Imp}_x)^2 + (\tilde{b}^{\rm Imp}_y)^2}$. Also shown in the figure are the radial coordinates $(b^{\rm Imp}_{x0}, b^{\rm Imp}_{y0})$ of the trajectory in $z = 0$ and, being that the trajectory is not a straight line, they differ from $(\tilde{b}^{\rm Imp}_x, \tilde{b}^{\rm Imp}_y)$. Without magnetic field $\tilde{b}^{\rm Imp}_x = b^{\rm Imp}_{x0}$ and $\tilde{b}^{\rm Imp}_y = b^{\rm Imp}_{y0}$.

When dealing with collisions of $P_s^*$ in magnetic field, we have adopted a definition of impact parameter $\tilde{b}^{\rm Imp}$ that has the property $\tilde{b}^{\rm Imp} \to b^{\rm Imp}$ when $B \to 0$, that is, it reproduces the standard definition for vanishing magnetic field.

Figure 15 shows a pictorial view of a the geometry of the collision in the presence of magnetic field. $\tilde{b}_{\rm Imp}$ is defined as the distance between the $P_s^*$ center-of-mass trajectory in the absence of interaction and the target antiproton evaluated in the plane $z = z^i_{\bar{p}}$. Figure 15 also shows $b_0^{\rm Imp}$ defined as the distance between the same $P_s^*$ center-of-mass trajectory and the $z$ axis evaluated in the plane $z = 0$. Note that $\tilde{b}^{\rm Imp}$ and $b_0^{\rm Imp}$ are in general different.

The cross-section results shown below have been calculated according to Eq. (8) using $\tilde{b}^{\rm Imp}$ as impact parameter. This is the same approach used in Ref. [16]. Precisely, we uniformly generated within a circle of radius $\tilde{b}^{\rm Imp}_{\rm max}$ the points with coordinates $(\tilde{b}^{\rm Imp}_x, \tilde{b}^{\rm Imp}_y)$ in the plane $z = z^i_{\bar{p}}$. After having performed the adiabatic switching of the magnetic field and the randomization we have placed the $P_s^*$ in the point $(\tilde{b}^{\rm Imp}_x, \tilde{b}^{\rm Imp}_y, z^i_{\bar{p}})$. Then we have followed the $P_s^*$ full motion back in time (setting $v_z^{\rm cm} < 0$ and changing the sign of velocities and the direction of the magnetic field) without interaction with the antiproton until it reaches the position $z = 0$. We call $(b^{\rm Imp}_{0x}, b^{\rm Imp}_{0y})$ the radial coordinates reached by the center of mass when $z = 0$. Then we inverted again the sign of the velocity, we restored the initial direction of the magnetic field, and we solved the three-body problem with the antiproton interaction switched on; the positronium starts from the position $(b^{\rm Imp}_{0x}, b^{\rm Imp}_{0y}, 0)$ with the rest of the kinematic variables resulting from the back propagation procedure.

As an example, Fig. 16 shows all the values of $b_0^{\rm Imp}$ obtained for each $b^{\rm Imp}$ with $n_{P_s} = 18$, $B = 1$ T directed along $z$ and $k_v = 0.015$.

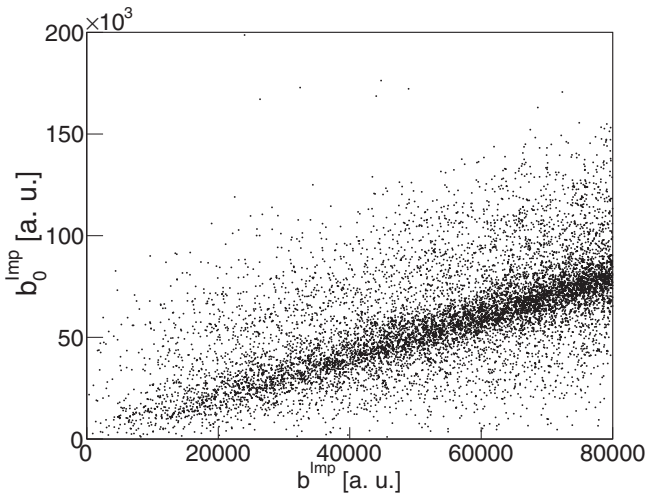


FIG. 16. Scatter plot of $b_0^{\mathrm{Imp}}$ vs $b^{\mathrm{Imp}}$ obtained with $n_{\mathrm{P}_s} = 18$, $B = 1$ T directed along $z$, $k_v = 0.015$, and method 2. The starting point of the $\mathrm{P}_s$ center-of-mass trajectory which is back tracked until it reaches $z = 0$ is uniformly generated within a circle with radius $b_{\mathrm{max}}^{\mathrm{Imp}} = 8\times10^4$ a.u.

### D. Cross-section results in magnetic field

We have calculated the charge-exchange cross section for some values of magnetic field of interest in antihydrogen experiments and for some reference values of $n_{\mathrm{P}_s}$. We have also studied the effect of the angle $\Theta_B$ of the magnetic field with respect to the positronium flight direction ($z$ axis).

Figures 17 and 18 compare the zero magnetic-field cross section normalized to $n_{\mathrm{P}_s}^4$ to the same quantity obtained for some reference values of $n_{\mathrm{P}_s}$ and two values of $B$ (1 and 2 T) with $\Theta_B = 0$. Note that the magnetic field not only breaks the universality of the shape of the normalized cross section as a function of $k_v$ shown in Fig. 2 but also it destroys the $1/k_v^2$ law. The curves describing $\sigma/n_{\mathrm{P}_s}^4$ versus $k_v$ in magnetic field cross the reference zero field curve when $k_v = k_v^X$. In Fig. 17, for example, $k_v^X \simeq 0.1(0.03)(0.02)$ if $n_{\mathrm{P}_s} = 27(18)(16)$ while if the $n_{\mathrm{P}_s} = 13$ then $k_v^X$ is lower than the values reported in the plot. There is an interesting range of positronium velocity

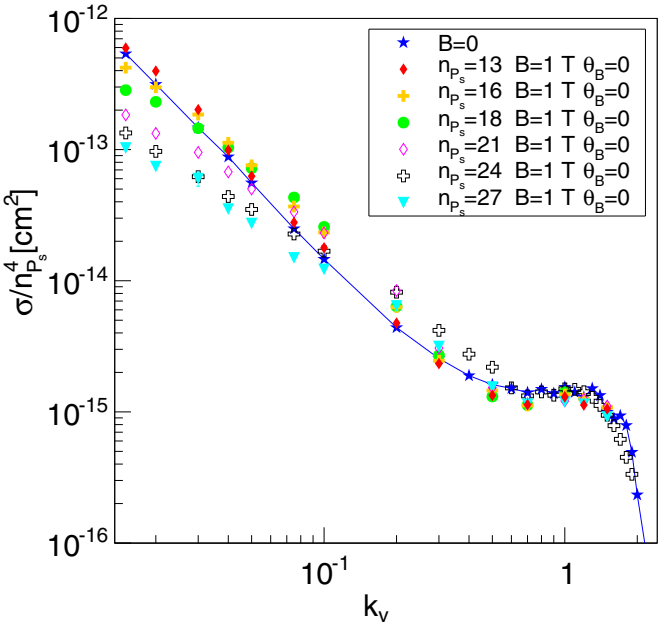


FIG. 17. Charge-exchange cross section divided for $n_{\mathrm{P}_s}^4$ as a function of $k_v$ calculated with $B = 1$ T, $\Theta_B = 0$, and with $n_{\mathrm{P}_s} = 13$, 16, 18, 21, 24, 27. For comparison the normalized zero magnetic-field cross section is reported (blue stars). Compare with Fig. 2.

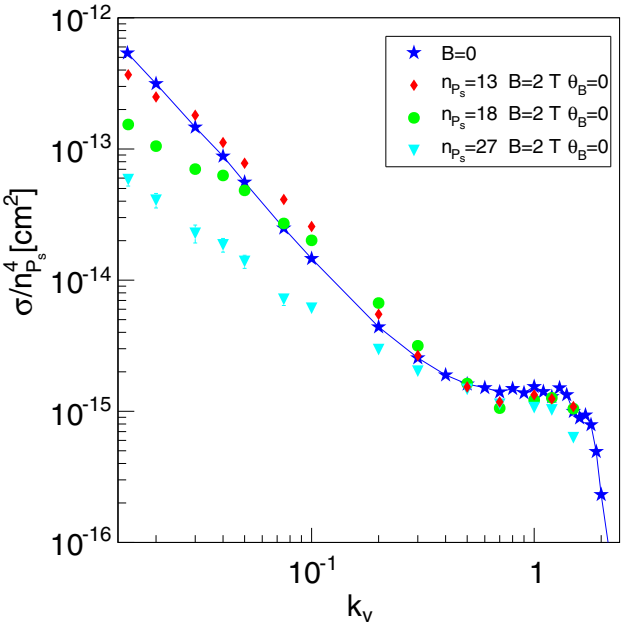


FIG. 18. Charge-exchange cross section divided for $n_{\mathrm{P}_s}^4$ as a function of $k_v$ calculated with $B = 2$ T, $\Theta_B = 0$, and with $n_{\mathrm{P}_s} = 13$, 18, 27. For comparison the normalized zero magnetic-field cross section is reported (blue stars). Compare with Fig. 2.

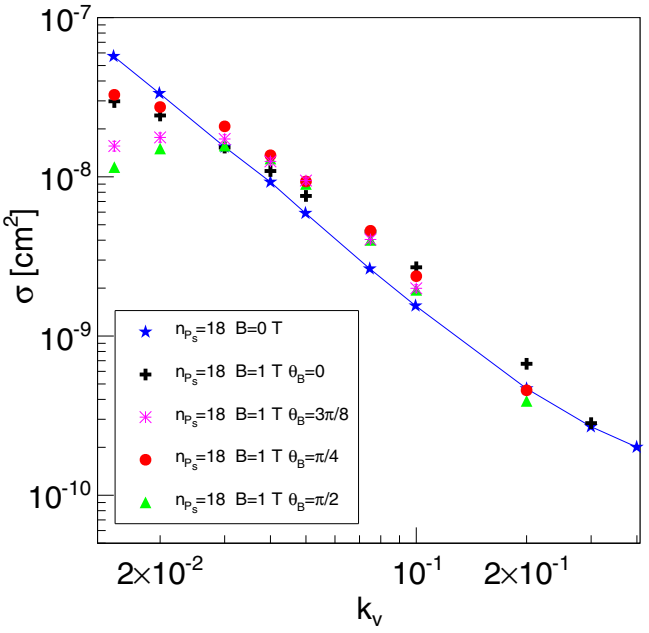


FIG. 19. Charge-exchange cross section calculated with $B = 1$ T for positronium with principal quantum number $n_{\mathrm{P}_s} = 18$ and four values of the angle $\theta_B$. For comparison the zero magnetic-field cross section is reported (blue stars).

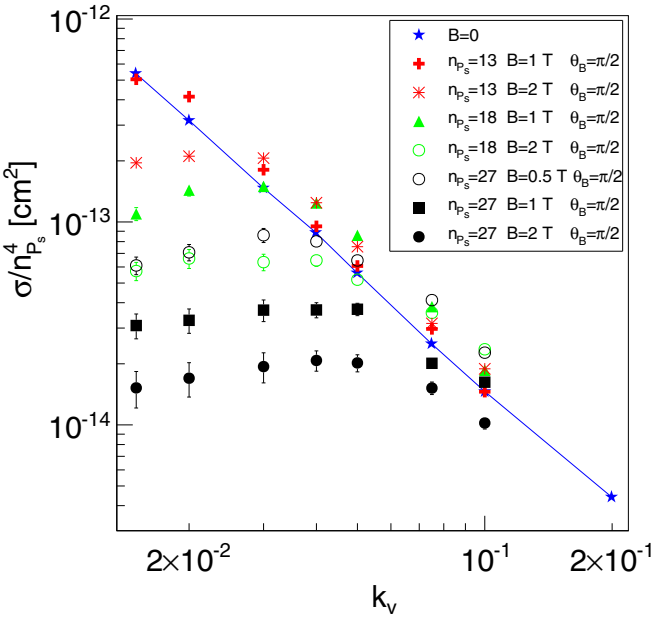


FIG. 20. Low velocity charge-exchange cross section calculated with interesting combinations of $B = 0.5, 1, 2$ T and $n_{P_s} = 13, 18, 27$ and $\theta_B = \pi/2$. For comparison the zero magnetic-field cross section is reported (blue stars).

satisfying $k_v > k_v^X$ where the charge-exchange cross section in magnetic field is slightly higher than that in the absence of field. However if $k_v < k_v^X$ then $\sigma/n_{P_s}^4$ in the presence of magnetic field significantly deviates from the $1/k_v^2$ law and it reaches values lower than the corresponding field-free ones. The comparison of the results of Figs. 17 and 18 indicates that $k_v^X$ is a function of both $B$ and $n_{P_s}$.

The low velocity reduction of the cross section also depends on the angle $\Theta_B$ thus making the $k_v^X$ value also a function of $\Theta_B$ with the maximum reduction with respect to the field-free case obtained when positronium flies perpendicular to the field. The dependance upon the angle clearly appears in Fig. 19 which compares the field-free cross section as a function of $k_v$ for $n_{P_s} = 18$ with that obtained with $B = 1$ T and some $\Theta_B$ values. Figure 20 compares the low velocity scaled cross section calculated with worst case angle $\theta_B = \pi/2$ and some values of magnetic field and $n_{P_s}$ and it shows how the deviation from the $1/k_v^2$ regime is influenced by these parameters.

### E. Asymmetry of the distribution of $\bar{H}$ angular momentum

The distribution of the principal quantum numbers of the antihydrogen and its velocity are not affected in a relevant way by the magnetic field. As already stated in Ref. [21], the magnetic field influences the distribution of the component of the angular momentum in the direction of the field and it favors the formation of antihydrogen in high field seeking states. Despite the slightly lower values of the magnetic field here considered, we obtain a result similar to that of [21] but our analysis as a function of the velocity of the incoming positronium shows that the effect is velocity dependent and it is strongly pronounced for $k_v$ values corresponding to the $1/k_v^2$ regime of the field-free cross section. Figure 21 compares some examples of distributions of the $z$ component of the canonical angular momentum $L_z = (x_{\bar{H}} v_{y\bar{H}} - y_{\bar{H}} v_{x\bar{H}}) + B(x_{\bar{H}}^2 + y_{\bar{H}}^2)$ of the antihydrogen formed with $\vec{B}$ directed along $z$ for high and low velocity of the positronium: though the effect depends on $n_{P_s}$ and $B$ in general the asymmetry of the $L_z$ distribution toward positive value is reduced if the collision velocity increases. The field-free distribution is symmetric.

## V. CONCLUSIONS

The charge-exchange reaction between Rydberg positronium and cold antiprotons is of high interest as it offers the possibility to obtain cold antiatoms with no energy externally supplied to the antiprotons during the formation process. In fact it can be experimentally implemented by preparing cold antiprotons in a trap and then letting the Rydberg positronium fly through them [2]. The temperature of the resulting antihydrogen is thus limited only by the antiproton temperature before the reaction and by the recoil energy. On the contrary in the antihydrogen formation by three-body recombination, the electrically charged antiprotons and positrons must be trapped using nested traps [37] and antiprotons are gently launched through the previously cooled positrons cloud. As result, antihydrogen is typically formed with energies higher than the the positron thermal energy because the antiprotons do not thermalize before the capture [21]. High Rydberg

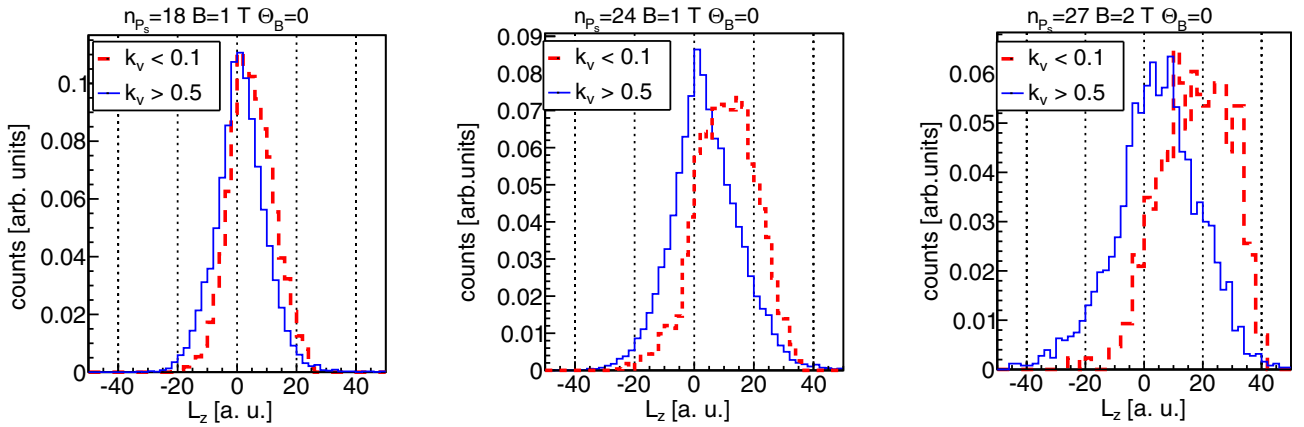


FIG. 21. Distributions of $L_z$ of antihydrogen produced with magnetic field along $z$. Without magnetic field the distribution is symmetric.

states of positronium are preferred in the charge-exchange process as the cross section is proportional to $n_{\mathrm{P}_s}^4$ and the recoil energy decreases while $n_{\mathrm{P}_s}$ increases. The results here reported suggest that charge exchange with $n_{\mathrm{P}_s}$ in the range 13–20, as foreseen for example in the AEgIS experiment, is a very effective channel for the production of antihydrogen with kinetic energy corresponding to about 100 mK or below.

In the absence of magnetic field, when the $\mathrm{P}_s$ center-of-mass velocity is reduced below about 0.2–0.3 times the classical velocity of the positron in the circular Kepler orbit, the cross section rises as $1/E_{\mathrm{P}_s}^{\mathrm{cm}}$. This work shows this behavior for Rydberg states of positronium. It is also interesting that the CTMC method gives results in fair agreement with the CCC quantum model for low $n_{\mathrm{P}_s}$ values ($n_{\mathrm{P}_s} < 3$) in the low velocity collision regime.

The low velocity behavior of the cross section is of high experimental interest and in fact efforts are already ongoing for producing cold positronium [38]. In the AEgIS scenario antiprotons are trapped and cooled in a Penning-Malmberg trap and antihydrogen is produced when Rydberg positronium traverses the antiproton cloud. Positronium atoms are formed by launching positrons towards a nanoporous target material where they lose their energy and bind with high probability to an electron. Positronium atoms cool by collisions with the pore walls until eventually they reach thermal equilibrium with the target. Once they emerge in vacuum they are excited to selected Rydberg states by laser pulses [39]. The velocity of the emerging positronium can be tailored by a proper selection of the materials used to build the target together with the optimization of its temperature and properties and finally by a suitable choice of the positron implantation energy [38]. With $n_{\mathrm{P}_s}$ in the range 13–20 the onset of the $1/E_{\mathrm{P}_s}^{\mathrm{cm}}$ regime is around 1 meV which represents an energy value well reachable with cryogenic (10 K) positronium formation targets. Colder targets can be operated with consequent slower emitted positronium. Progress toward laser cooling of positronium outside the target [40,41] are of great interest as a further method to obtain large samples of very cold $\mathrm{P}_s$.

A magnetic field is unavoidable in the present experimental antihydrogen setup as it is needed to trap and manipulate antiprotons. Our CTMC studies showed that in the presence of magnetic field there is a value of $k_v^X$ below which the cross section does not follow $1/E_{\mathrm{P}_s}^{\mathrm{cm}}$ law when the $\mathrm{P}_s$ velocity is reduced. When $k_v < k_v^X$ the cross section in presence of magnetic field is lower than the field free one. $k_v^X$ depends on the value of $B$, $n_{\mathrm{P}_s}$, $\Theta_B$. Our results show that the effect is tolerable if the magnetic field is kept around 1 T or below as expected in Ref. [2] and if $n_{\mathrm{P}_s} < 18$–20. Particularly interesting is also the increase of the charge-exchange cross section for $k_v > k_v^X$.

We showed that the dynamics of charge-exchange process is affected by the angle $\Theta_B$ between the magnetic field and the flight direction of the incoming positronium. This effect produces a dependance of the cross section upon $\Theta_B$ which is significant even at moderate magnetic fields of 1–2 T; our results suggest that these effects should become more prominent at higher field values.

## ACKNOWLEDGMENT

This work was supported by Istituto Nazionale di Fisica Nucleare (INFN-Italy).

[1] E. Widmann, R. S. Hayano, M. Hori, and T. Yamazaki, Nucl. Instrum. Methods Phys. Res., Sect. B **214**, 31 (2004).
[2] M. Doser *et al.* (AEgIS Collaboration), Class. Quantum Grav. **29**, 184009 (2012).
[3] K. A. Olive *et al.* (Particle Data Group), Chin. Phys. C **38**, 090001 (2014).
[4] J. D. Tasson, Rep. Prog. Phys. **77**, 062901 (2014).
[5] C. Parthey *et al.*, Phys. Rev. Lett. **107**, 203001 (2011).
[6] A. Peters, K. Y. Chung, and S. Chu, Nature (London) **400**, 849 (1999).
[7] M. Amoretti *et al.* (ATHENA Collaboration), Phys. Lett. **B578**, 23 (2004).
[8] M. Amoretti *et al.* (ATHENA Collaboration), Nature (London) **419**, 456 (2002).
[9] G. Gabrielse *et al.* (ATRAP Collaboration), Phys. Rev. Lett. **89**, 213401 (2002).
[10] G. B. Andresen *et al.* (ALPHA Collaboration), Nature (London) **468**, 673 (2010).
[11] G. Gabrielse *et al.* (ATRAP Collaboration), Phys. Rev. Lett. **108**, 113002 (2012).
[12] N. Kuroda *et al.* (ASACUSA Collaboration), Nat. Commun. **5**, 3089 (2014).
[13] P. Perez and J. Sacquin, Class. Quantum Grav. **29**, 184008 (2012).
[14] M. Amoretti *et al.* (ATHENA Collaboration), Phys. Lett. B **583**, 59 (2004).
[15] C. H. Storry *et al.* (ATRAP Collaboration), Phys. Rev. Lett. **93**, 263401 (2004).
[16] J. Lu, E. Y. Sidky, Z. Roller-Lutz, and H. O. Lutz, Phys. Rev. A **68**, 024702 (2003).
[17] J. Shertzer, J. Ackermann, and P. Schmelcher, Phys. Rev. A **58**, 1129 (1998).
[18] A. S. Kadyrov *et al.*, Phys. Rev. Lett. **114**, 183201 (2015).
[19] C. M. Rawlins *et al.*, Phys. Rev. A **93**, 012709 (2015).
[20] E. A. Hessels, D. M. Homan, and M. J. Cavagnero, Phys. Rev. A **57**, 1668 (1998).
[21] M. L. Wall, C. S. Norton, and F. Robicheaux, Phys. Rev. A **72**, 052702 (2005).
[22] G. Testera *et al.*, in *Proceedings of the Workshop on Cold Antimatter Plasmas and Application to Fundamental Physics*, edited by Y. Yasunori and K. Yamazaki, AIP Conf. Proc. No. 1037 (AIP, Melville, NY, 2008), p. 5.
[23] R. Abrines and I. C. Percival, Proc. Phys. Soc. **88**, 861 (1966).
[24] R. Abrines and I. C. Percival, Proc. Phys. Soc. **88**, 873 (1966).
[25] R. E. Olson, Phys. Rev. A **24**, 1726 (1981).
[26] R. E. Olson, in *Springer Handbook of Atomic, Molecular and Optical Physics*, edited by G. W. F. Drake (Springer Science and Business Media, New York, 2006), p. 869.

[27] R. L. Becker and A. D. MacKellar, J. Phys. B **17**, 3923 (1984).
[28] J. E. Avron *et al.*, Ann. Phys. **114**, 431 (1978).
[29] P. Schmelcher, J. Phys. B **25**, 2697 (1992).
[30] T. Pohl, H. R. Sadeghpour, and P. Schmelcher, Phys. Rep. **484**, 181 (2009).
[31] H. Friedrich and D. Wintgen, Phys. Rep. **183**, 37 (1989).
[32] E. A. Solov'ev, Sov. Phys. JETP **48**, 635 (1978).
[33] R. T. Skodje, F. Borondo, and W. P. Reinhardt, J. Chem. Phys. **82**, 4611 (1985).
[34] E. A. Solov'ev, Eur. Phys. J. D **65**, 331 (2011).
[35] S. Bradenbrink *et al.*, Phys. Rev. A **55**, 4290 (1997).
[36] J. Taylor, *Classical Mechanics* (University Science Books, Sausalito, CA, 2005).
[37] G. Gabrielse, L. Haarsma, S. Rolston, and W. Kells, Phys. Lett. A **129**, 38 (1988).
[38] S. Mariazzi *et al.*, Phys. Rev. B **81**, 235418 (2010).
[39] S. Aghion *et al.* (AEgIS Collaboration), Phys. Rev. A **94**, 012507 (2016).
[40] P. Yzombard *et al.* (AEgIS Collaboration), *Proceedings of 12th International Conference on Low Energy Antiproton Physics* (LEAP 2016), JPS Conf. Proc. (to be published).
[41] T. Kumita *et al.*, Nucl. Instrum. Methods Phys. Res., Sect. A **192**, 171 (2002).